Revisiting the 1992 Landers earthquake: a Bayesian exploration of co-seismic slip and off-fault damage

B. Gombert[1], Z. Duputel[1], R. Jolivet [2], C. Doubre [1], L. Rivera[1] and M. Simons[3]

[1] *Institut de Physique du Globe de Strasbourg, UMR7516, Université de Strasbourg, EOST/CNRS*
[2] *Laboratoire de géologie, Département de Géosciences, École Normale Supérieure,*
PSL Research University, CNRS UMR, Paris, France
[3] *Seismological Laboratory, Geological and Planetary Sciences, California Institute of Technology,*
Pasadena, California, USA

SUMMARY

Existing models for the distribution of subsurface fault slip associated with the 1992 Landers (CA) earthquake (Mw = 7.3) show significant dissimilarities. In particular, they exhibit different amounts of slip at shallow depths (< 5km). These discrepancies can be primarily attributed to the ill-posed nature of the slip inversion problem and to the use of physically unjustifiable smoothing or regularization constraints. In this study, we propose a new coseismic model obtained from the joint inversion of multiple observations in a relatively unregularized and fully Bayesian framework. We use a comprehensive dataset including GPS, terrestrial geodesy, multiple SAR interferograms and co-seismic offsets from correlation of aerial images. These observations provide dense coverage of both near- and far-field deformation. To limit the impact of modeling uncertainties, we develop a 3D fault geometry designed from field observations, co-seismic offsets and the distribution of aftershocks. In addition, we account for uncertainty in the assumed elastic structure used to compute the Greens functions. Our solution includes the ensemble of all plausible models that are consistent with our prior information and fit the available observations within data and prediction uncertainties. Using near-fault high-resolution ground deformation measurements and the density of aftershocks, we investigate the properties of the damage zone and its impact on the inferred slip at depth. We attribute a part of the inferred slip deficit at shallow depth to our models not including the impact of a damage zone associated with a reduction of shear modulus in the vicinity of the fault.

Key words: Inverse theory; Probability distributions; Earthquake source observations; Fractures, faults, and high strain deformation zones

1 INTRODUCTION

Following the 1979 Imperial Valley earthquake more than three decades ago (Olson & Apsel 1982, Hartzell & Heaton 1983), finite-fault source models have been routinely constructed after most significant earthquakes. Despite the increasing volume and quality of available geodetic and seismological data, we still observe a significant variability in inferred subsurface fault slip for a given event. Estimating the distribution of fault slip from surface deformation is fundamentally an ill-posed inverse problem with different models that can fit the data equally well. Therefore, different finite-fault models for the same earthquake often display significant dissimilarities.

Over the past decade, there have been considerable efforts in the seismological community to study this problem and characterize the variability of the models (e.g., Mai et al. 2016). Furthermore, data and forward predictions are imperfect and the corresponding uncertainties are often difficult to account for. A standard approach to overcome the non-uniqueness of the solution relies on Tikhonov regularization (e.g. Hansen 1998) involving minimization of first or second order spatial derivatives of the slip model to enforce smoothness of the slip distribution. However, various regularization strategies can affect the solution. The impact of different approaches to regularization, coupled with the lack of consideration of model un-

certainties, can hamper our ability to draw clear conclusions about earthquake source processes.

Due to the availability of a comprehensive dataset, many finite-fault models have been published for the 1992 $M_w = 7.3$ Landers earthquake (e.g., Murray et al. 1993, Cohee & Beroza 1994, Hudnut et al. 1994, Freymueller et al. 1994, Wald & Heaton 1994, Cotton & Campillo 1995, Fialko 2004*b*, Xu et al. 2016). Common patterns emerge in the inferred slip distributions including the fact that most of the slip occurred in the central section of the rupture (i.e., the Homestead Valley Fault). However, there are also clear inconsistencies. In particular, published studies have inferred shallow slip to vary between 30% and 112% of the slip inferred at 7 km depth. Since there is no indication of large inter- or post-seismic slip at shallow depth (Fialko 2004*a*, Shen et al. 1994, Savage & Svarc 1997), the amount of the potential shallow co-seismic slip deficit has an impact on seismic risk assessment as this suggests that part of the accumulated strain is not released by the earthquake (Simons et al. 2002, Fialko et al. 2005). Simons et al. (2002) and Kaneko & Fialko (2011) suggested that such deficits might be an artifact due to inelastic response of the medium in the vicinity of the fault. Inelasticity would bias slip models where observations at short distances are modeled assuming elastic Green's functions. An apparent shallow slip deficit could also be caused by smoothing constraints and sparseness of near-fault data (Simons et al. 2002, Xu et al. 2016). Finally, unaccounted heterogeneities in the crust elastic properties can also result in a biased slip distribution at depth (Barbot et al. 2008). One way to evaluate these hypothesis is to derive all the models consistent with the available data without arbitrary regularization of the inverse problem and explore the potential mechanisms statistically.

We perform a Bayesian exploration of the 1992 Landers rupture to evaluate the population of plausible slip models given geodetic data and forward problem uncertainties. Our approach is exempt from any smoothing and allows us to assess the extent of any purported shallow slip deficit as constrained by available geodetic data. Using near-fault data, we also investigate the impact of lateral heterogeneities on the inferred slip distribution at depth.

2   DATA OVERVIEW

We use a large geodetic dataset composed of GPS measurements at 82 sites, 23 trilateration measurements, 2 SAR interferograms and 14 optical correlation images. This combination of data provides good coverage in both the near- and far-fields.

2.1   GPS and trilateration data

We use 3-component observations from 82 GPS stations scattered across southern California (Hudnut et al. 1994) with a few stations in the vicinity of the fault (Figs 1 and 2). Observations of the vertical component of displacement is associated with significantly larger uncertainties than the horizontal components. In addition, a trilateration network covers the southern part of the rupture (Figs 1 and 2). We invert directly the horizontal relative line-length changes provided by Murray

et al. (1993) instead of the pre-inverted displacement vectors of the trilateration stations. The GPS and trilateration data include up to a few months of inter-seismic and post-seismic deformation. However, the associated post-seismic displacements measured by GPS are expected to be less than ∼10 cm, which is substantially smaller than the ∼8 m of co-seismic displacement observed near the earthquake rupture. (Murray et al. 1993, Peltzer et al. 1998).

2.2   InSAR data

We use two SAR interferograms computed from pre- and post-earthquake acquisitions on both ascending and descending tracks of the ERS satellite (Fig. 1(b)). Interferograms are computed using the ROI_PAC software (Rosen et al. 2004). We downsample the unwrapped interferograms using a recursive quad-tree algorithm (Simons et al. 2002, Lohman & Simons 2005) to reduce the number of observation points. The final downsampled ascending and descending interferograms contain 730 and 663 pixels, respectively. Downsampled observations, predictions, and residuals are shown in Fig. S1 available in the electronic supplement. Using the procedure described by Jolivet et al. (2014) for each InSAR scene, we estimate an empirical data covariance function, which statistically represents atmospheric noise. We find standard deviations of 3.5 cm and 0.9 cm for the descending and ascending tracks, respectively. The correlation length is 11 km for both images. Covariance functions are shown in Fig. S2. While the second image of the interferogram on the ascending track was acquired only two days after the mainshock, the interferogram on the descending track includes more than one month of post-seismic deformation.

2.3   Optical correlation images

We use optical correlation images of the ground displacement from Ayoub et al. (2009). Maps of ground displacement are made using 14 pairs of aerial photographs acquired before and after the earthquake. Cross-correlation is performed to derive horizontal co-seismic displacements in the vicinity of the fault. Pre-earthquake photographs were acquired during the summer 1989 while post-earthquake were acquired during the autumn 1995. The footprint of each pair is slightly less than 10 x 10 km^2 and the dataset covers almost the entire surface rupture of the fault (Figs 2 and 7(a)). Because of their near-field coverage, optical data can finely constrain shallow slip in our models. However, as pointed out by Kaneko & Fialko (2011), near-fault observations may include inelastic effects that can bias slip estimates assuming linear elasticity. To avoid such artifact, we remove any near-fault pixels within 300 m of the fault. This cut-off length is in agreement with measurements by Milliner et al. (2015) showing that off-fault deformation is generally limited to a narrow zone around the fault (with an average half-width smaller than 80 m). Removing data in the vicinity of the fault also reduces the impact of modeling errors due to fault parameterization. Indeed, the assumption of constant slip in fault patches and the discretization of the fault trace (every ∼1.5 km) induce artifacts in the predicted deformation field very close to the fault (See supporting informa-
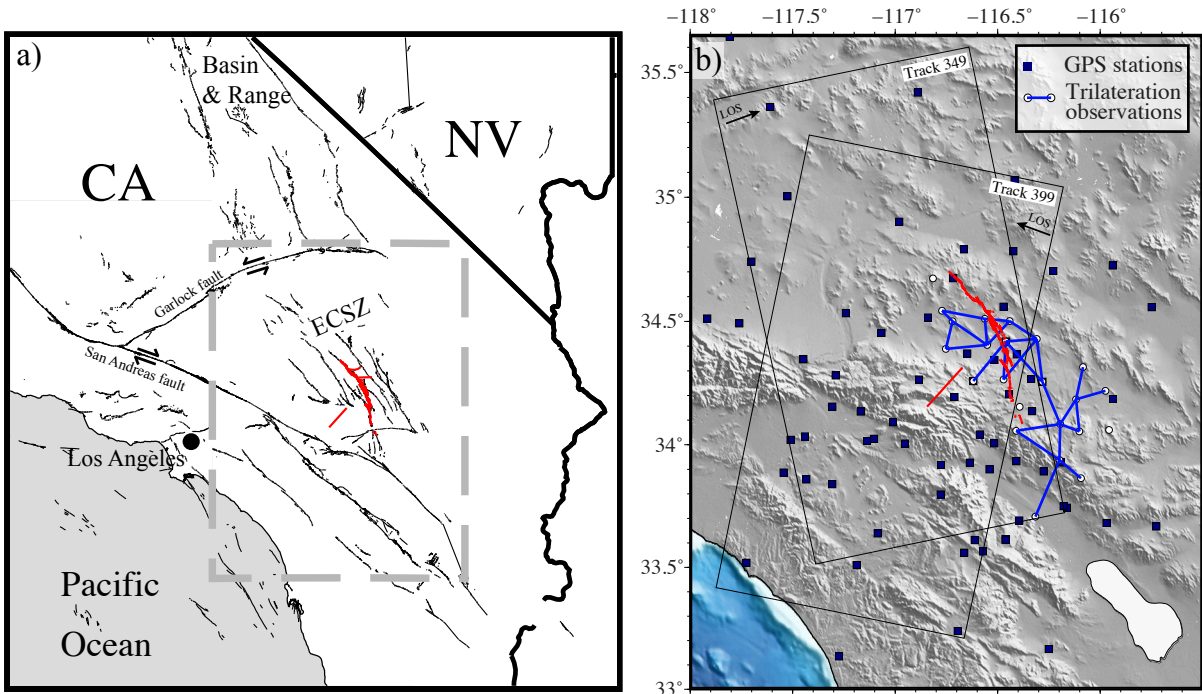
Figure 1. General overview of the area. (a) Tectonic context of Southern California. The dashed grey rectangle shows the extent of (b). The Landers earthquake surface rupture is plotted in red. The faults involved are part of the Eastern California Shear Zone (ECSZ). **(b)** Far-field observations used in this study. The thin black rectangles illustrate the InSAR track footprints. The ascending interferogram (Track 349) covers the time span between 26 May to 30 June 1992 and the descending interferogram (Track 399) between 24 April to 7 August. Topography is from the Space Radar Topographic Mission (SRTM) database.

tion T1 and Fig. S3). In addition, using the same technique as for InSAR data in section 2.2, each image is downsampled and data covariance is estimated using empirical covariograms. The resulting standard deviation is typically around 30 cm and the correlation length ranges from 300 m to 1 km. Most of the post-seismic deformation is included in the timespan separating the two acquisitions (Fialko 2004*a*). However, as mentioned by Milliner et al. (2015), the detection threshold of optical image correlation is about 10 cm, suggesting that ~15 cm of near-field post-seismic deformation lie in the uncertainties of the measurement.

3 PROBABILISTIC SLIP INVERSION

3.1 Model parametrization

While most previous studies used relatively simplified linear geometries, our fault parametrization shown in Fig. 3 consists of nine segments following the surface rupture trace. The three main segments are the Johnson Valley, Homestead Valley, and Emerson and Camp Rock faults (Sieh et al. 1993). Those three segments are linked by two small junctions and completed by the small Galway Lake Fault in the northern part of the rupture. In addition, we parametrize two antithetic faults on the eastern side of the Emerson segment. These two faults were not directly mapped by Sieh et al. (1993) but have been previously incorporated as linear segments by Fialko (2004*b*) from

the distribution of aftershocks. In the present study, the northern antithetic segment is refined as a curved fault from the detailed analysis of InSAR ground deformation profiles along with the Hauksson et al. (2012) relocated earthquake catalog (see Fig. 3). Finally, we use an additional fault corresponding to the $M_w = 6.5$ Big Bear aftershock, which orientation is derived from the Hauksson et al. (2012) catalog. Consistent with Fialko (2004*b*), faults segments are assumed to be vertical and to extend down to 15 km. Although this depth is roughly in agreement with the maximum depth of aftershock, we cannot exclude a more complex geometry at depth as often reported when multiple fault segments interact (Segall & Pollard 1980). To evaluate the effect of such complexities, we propose an alternative geometry in which shallow parallel branches merge on a single deeper segment. This geometry is similar to a flower structure that can be observed in some strike-slip faults (e.g., Zigone et al. 2015).

For both assumed fault geometries, each segment is discretized in four rows of subfaults extending down to 1.5 km, 4.5 km, 9.0 km, and 15.0 km depth. The size of each subfault is designed to have an acceptable resolution at depth (resolution $R \geq 0.8$ as defined in the Supplementary Material for the strike-slip component, see Fig. S4). This strategy ensures small posterior model uncertainty but more importantly, it enables good convergence of the Bayesian sampling algorithm used for the inversion.
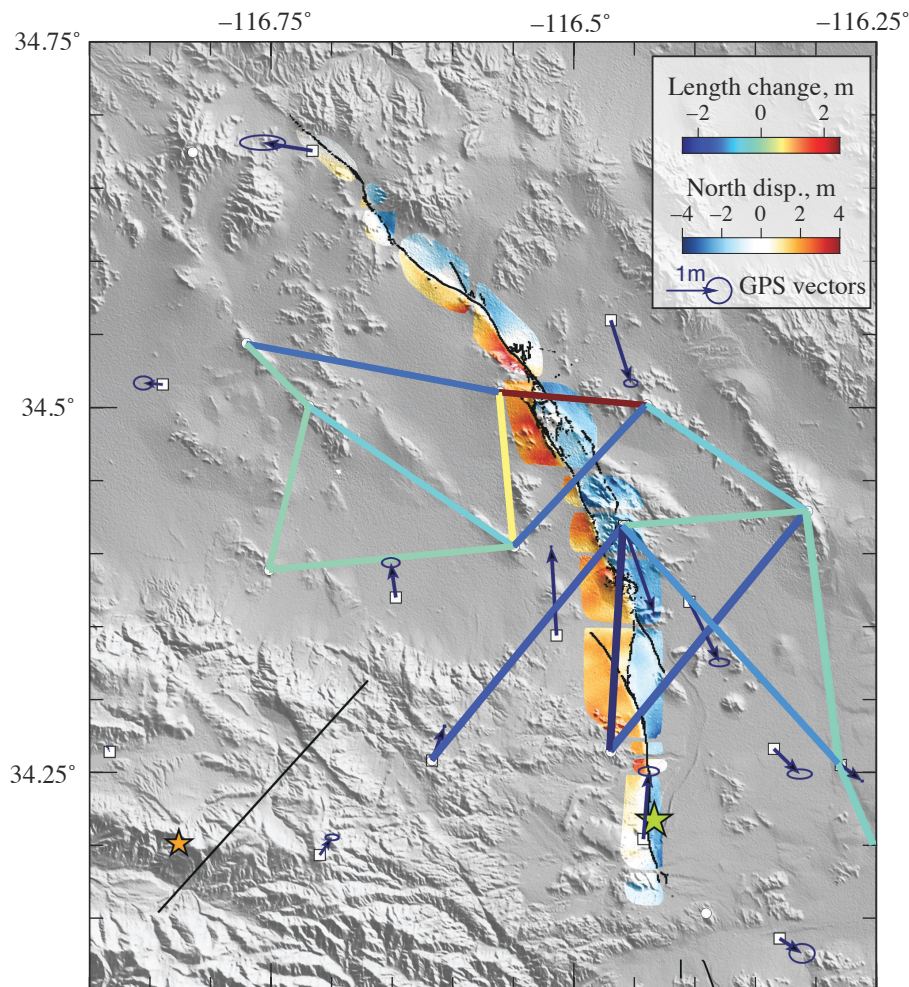
Figure 2. Near field observations. Lines are colored according to length changes in the trilateration network. The optical correlation mosaic is plotted around the fault trace from (Sieh et al. 1993). Mainshock and Big Bear aftershock (M_w = 6.5) hypocentres from the Southern California Earthquake Center are indicated with a green and an orange star, respectively.

3.2 Bayesian sampling

We use a Bayesian approach to obtain the full posterior probability density function (PDF) of the slip distribution given the observations and uncertainties. According to the Bayes-Laplace theorem, we write the posterior PDF as:

$$p(\mathbf{m}|\mathbf{d}_{\text{obs}}) \propto p(\mathbf{m}) \exp\left[-\frac{1}{2}(\mathbf{d}_{\text{obs}} - \mathbf{Gm})^{\text{T}}\mathbf{C}_\chi^{-1}(\mathbf{d}_{\text{obs}} - \mathbf{Gm})\right]$$

(1)

where $\mathbf{m}$ is the model vector, $p(\mathbf{m})$ is the prior distribution, $\mathbf{d}_{\text{obs}}$ is the data vector, $\mathbf{G}$ is the Green functions matrix, and $\mathbf{C}_\chi$ is the misfit covariance describing both data and forward prediction uncertainties. We compute the Greens functions for a semi-infinite stratified elastic medium using the EDKS software (Zhu & Rivera 2002)

To sample the model space we use AlTar, a parallel Markov Chain Monte Carlo (MCMC) algorithm based on the CATMIP formalism (Minson et al. 2013). Using multiple MCMC chains in parallel, AlTar initially samples the prior PDF, $p(\mathbf{m})$, and then slowly increases the information brought by the data until it samples the posterior PDF. The implementation benefits from the use of high efficiency Graphic Processing Units (GPUs), allowing us to run more than 500 000 chains in parallel. Our final solution consists of an ensemble of models that are statistically distributed according to the posterior PDF. No spatial smoothing constraint is used in this procedure. We adopt different priors for the two different slip directions. The strike-slip component prior is a uniform PDF between -1 m and 30 m, hence promoting right-lateral faulting. The dip-slip prior is a Gaussian PDF centered on 0 m with a standard deviation of 5 m.

3.3 Model prediction uncertainties

Accounting for uncertainties in our forward predictions uncertainties is crucial since they correspond to one of the largest sources of variability between published slip models. Moreover, these uncertainties are important in our Bayesian framework as we do not use smoothing regularization. The model prediction uncertainties are described by the matrix $\mathbf{C}_{\text{p}}$, which
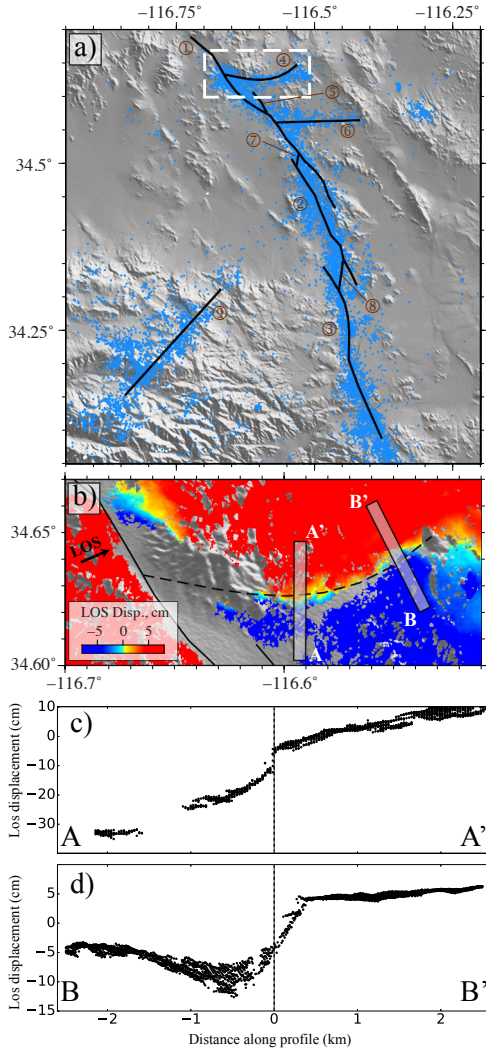
models in the source region along with the distribution of 3D velocity models from Kohler et al. (2003), as shown in Fig. S5.

3.4 Probabilistic slip model

Using our Bayesian framework, we generate 500 000 models representing our posterior information on slip distribution given available geodetic data. To interpret this ensemble, we need to extract a representative model and the corresponding uncertainties. In Fig. 4, we show the posterior mean model (i.e., the average of all sampled models) along with 95% confidence ellipses. A more detailed view is available in Fig. S6. The posterior mean model is a common choice as the Bayesian approach encourages one to think in terms of an ensemble solution instead of one single model. However, as shown in Fig. S7, other models can also be depicted such as the maximum a posteriori model (i.e., the mode of the posterior distribution) or the best fitting model (i.e., the sample in our population having the maximum posterior value). In our case, the maximum a posteriori model is insignificantly different to the posterior mean model since most marginal PDFs are nearly Gaussians (cf., Supporting text T2).

The results in Fig. 4 are based on vertical fault segments. They can be compared with the solution in Fig. S8 obtained assuming a more complicated flower parameterization introduced in section 3.1. Despite different fault dips, the inferred slip distributions are fairly similar in both geometries, showing the lack of sensitivity to the parametrization at depth. Although posterior PDFs of both geometries generally overlap in fault patches with large slip, we still observe significant differences as shown in Fig. S8. This suggests that modelling uncertainties included in $\mathbf{C}_P$ are still underestimated as we only incorporate Earth model uncertainties and neglect errors in the fault parameterization. In the following, we focus on the results obtained using vertical fault segments.

As expected, we observe predominately strike-slip motion along the entire fault system. Most of the slip concentrates along the central and northern parts of the rupture, with a peak amplitude of ∼11 m. These features are to first order comparable to previous results, although published models have lower peak slip amplitudes (e.g. Cohee & Beroza 1994, Fialko 2004b, Xu et al. 2016). This difference is probably due to smoothing imposed in previous studies that decreases the maximum slip amplitude. The two small junctions (shown in Fig. S6) show relatively large slip at depth, although they are associated with significant posterior uncertainties. In addition, these estimates are associated with significant along-dip correlation of slip amplitudes (cf., Fig. S9).

The model predictions reproduce the observations reasonably well. The performance of the models for GPS and trilateration data is presented in Fig. 5 with associated posterior uncertainties. Posterior mean InSAR predictions and residuals are shown in Fig. 6 in high-resolution, and decimated in Fig. S1. In high-resolution, we observe some moderate residuals in the vicinity of the fault, mainly due to the finiteness of the fault patches. Some larger wavelength residuals are visible on the southern part of the descending track. We suspect that this signal originates from post-seismic deformation (Fialko 2004a) as the second pass of this track is 5 weeks after the
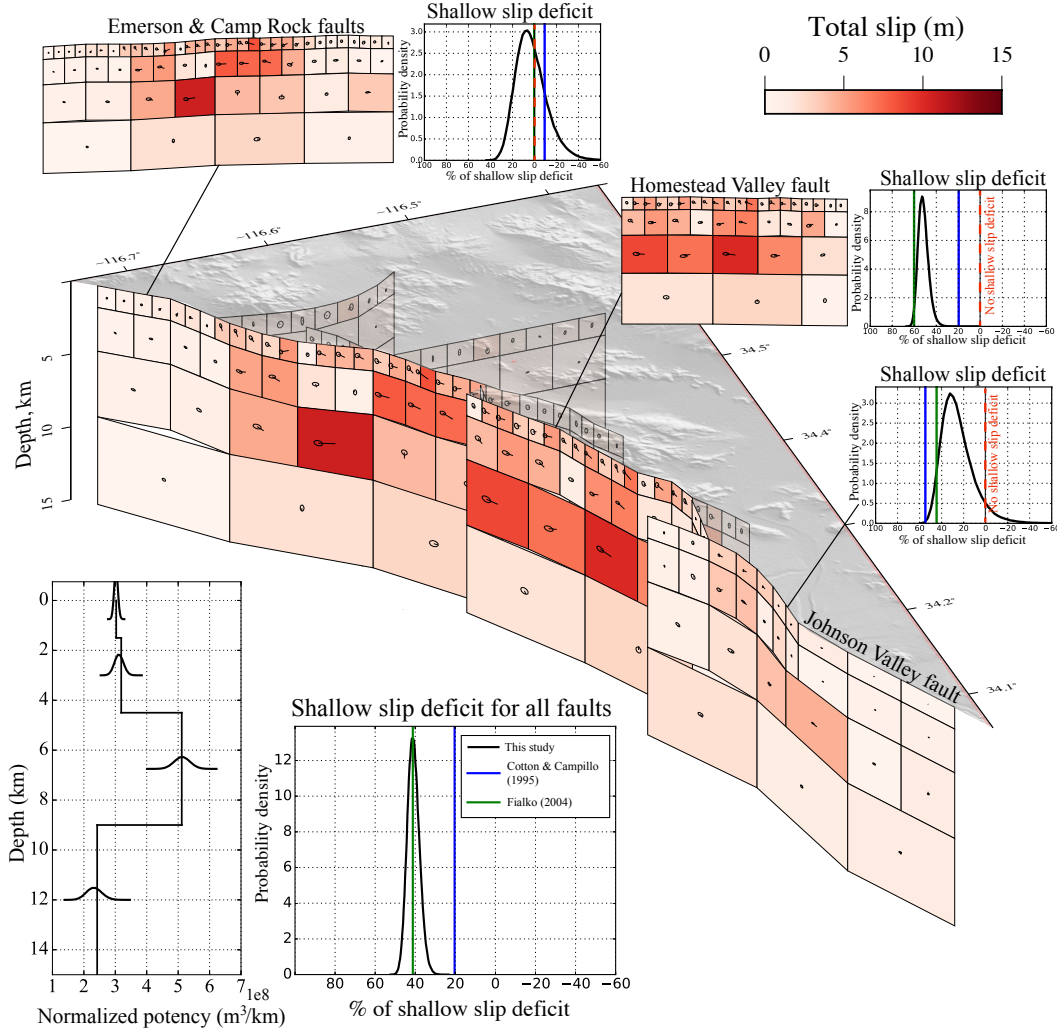

Figure 3. (a) Surface trace of the parametrized fault segments. Each segment is plotted as a thick black line. 1. Emerson and Camp Rock Faults, 2. Homestead Valley Fault, 3. Johnson Valley Fault, 4. Northern conjugate Fault, 5. Galway Lake Fault, 6. Southern conjugated Fault, 7. Emerson-Homestead Valley junction, 8. Kickapoo Fault, 9. Big Bear Fault. Blue dots represent aftershock locations from Hauksson et al. (2012). Dashed white rectangle shows the extent of (b). **(b)** Surface trace of the northern conjugate segment (dashed line). Rectangles show the position of the profiles shown in (c) and (d). Background color represents the InSAR ascending track LOS displacement pattern. **(c)** and **(d)** InSAR data profiles A-A' and B-B'

is added to the observation uncertainties matrix $\mathbf{C}_d$ to obtain the misfit covariance:

$$\mathbf{C}_\chi = \mathbf{C}_d + \mathbf{C}_p \qquad (2)$$

We build $\mathbf{C}_P$ using the approach of Duputel et al. (2014) to account for uncertainties in the elastic model used to compute the Green's functions. The layered elastic model used in this study is derived from the Southern California Earthquake Center 3D velocity model (Kohler et al. 2003). Uncertainties on the elastic parameters are inferred by comparing different

Figure 4. Posterior mean co-seismic slip model. The color of each subfault patch indicates the slip amplitude. Arrows and their associated 95% confidence ellipse indicate the slip direction and uncertainty. The bottom left inset shows the potency normalized by patch row width as a function of depth. PDFs of shallow slip deficit (SSD) are presented for the entire fault system and for individual fault segments. Vertical lines on the same plots indicate the SSD of two published models (Cotton & Campillo 1995, Fialko 2004*b*).

mainshock. Finally, our model explains reasonably well the optical correlation images despite large uncertainties associated with this dataset (Fig. 7). We also computed an equivalent moment tensor and centroid location and tested it against long period seismological observations (details are provided in the Supporting text T3 and Figs. S10, S11, and S12.)

3.5   Shallow slip deficit

A shallow slip deficit is commonly observed for large strike-slip earthquakes (Simons et al. 2002, Fialko et al. 2005). Although, in a simple linear elastic model, a uniform slip distribution at depth is expected when averaged over many seismic cycles (Tse & Rice 1986), this deficit does not seem to be recovered by either inter-seismic creep or post-seismic deformation (Fialko 2004*a*). Some exceptions with no detectable shallow slip deficit have nonetheless been documented such as

the 2013 $M_w = 7.7$ Balochistan earthquakes (Jolivet et al. 2014, Vallage et al. 2015).

Although a shallow slip deficit is observed in most published models of the Landers earthquake, there is a large variability in the actual amount of shallow slip deficit between different inversion results. To investigate this, we compute the normalized potency as a function of depth:

$$P_k = \frac{\sum_i \Delta u_{ik} \times A_{ik}}{w_k} \qquad (3)$$

where Δu_{ik} is the slip inferred in a patch of area A_{ik} and width w_k located in the k-th row and at an along-strike position i. This formulation allows us to avoid any bias due to the increase of patch size with depth. As shown in Fig. 4, we find a maximum potency on the 3rd row of patches (i.e., between 4.5 and 9 km depth, consistent with Simons et al. (2002)) that is nearly 1.7 times larger than surface estimates (i.e., at depth be-
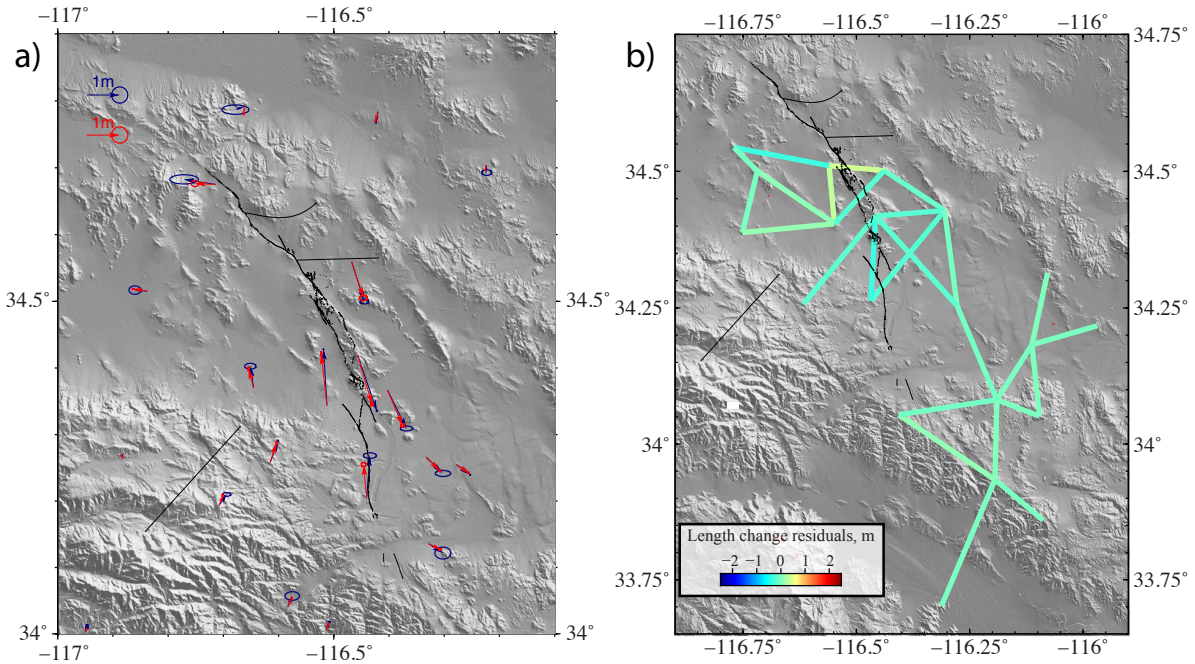
Figure 5. Model performance for GPS and trilateration data. (a) GPS observations (blue) and predictions (red) with their 1-sigma error ellipses. **(b)** Length changes residuals for the posterior mean model.

tween 0 and 1.5 km). To highlight this for individual fault segments, we define the percentage of shallow slip deficit (SSD) as:

$$SSD = 100 \left(\frac{P_{k=3} - P_{k=1}}{P_{k=3}} \right) \quad (4)$$

According to this definition, $SSD > 0$ indicates some amount of shallow slip deficit while $SSD \leq 0$ means that potency is equal or larger at the surface than at depth (i.e., no shallow slip deficit). The posterior distribution of SSD is shown in Fig. 4 for the three main fault segments and the overall rupture. Results and probability estimates are also summarized in Table 1.

Although the overall rupture depicts a shallow slip deficit of about 41%, we find different behaviors for different fault segments. We observe the smallest deficit along the Emerson and Camp Rock segment where the probability of shallow slip deficit is only 0.62. The Johnson Valley fault is more likely to present a shallow deficit, but the SSD is relatively moderate (SSD~25%). The largest deficit is measured for the Homestead Valley fault where the mean SSD is 52% with a probability close to 1 that the deficit is larger than 25%. The remaining fault segments are either too small, with too large uncertainties or did not slip enough to contribute significantly to the overall rupture estimate.

4 DISCUSSION

As pointed out in Section 1, previously published models differ, in particular regarding the amount of shallow slip deficit. A detailed comparison between our solution and previous models is provided in Fig. 4 and S13. The SSD values for previously published models extend from 70% (i.e. a large shallow slip deficit) to -12% (shallow slip exceeds slip at 7 km depth). Our slip deficit is thus smaller than some models (e.g., Zeng & Anderson 2000) but larger than others (e.g., Cotton & Campillo 1995, Wald & Heaton 1994, Cohee & Beroza 1994, Hernandez et al. 1999). Overall, there is a fairly good agreement with the model of Fialko (2004b) which closely matches our estimate of slip deficit. Unlike most of these previous models, our inversion includes near-field optical images which give a solid constraint on slip along the shallow part of the fault, hence improving our estimates of SSD. This is presented in Fig. S14 showing slip posterior uncertainties obtained with and without incorporating optical images, illustrating their significance in our inversion.

To assess the impact of smoothing constraints on the shallow slip deficit, we also performed damped least squares inversions incorporating a 2nd order Tikhonov regularization minimizing the roughness of the slip model $\mathbf{m_{est}}$ (Segall & Harris 1987, Ortega 2013):

$$\mathbf{m_{est}}(\epsilon) = \left(\mathbf{G}^{\mathrm{T}} \mathbf{C}_\chi{}^{-1} \mathbf{G} + \left(\epsilon \nabla^2 \right)^2 \right)^{-1} \mathbf{G}^{\mathrm{T}} \mathbf{C}_\chi \mathbf{d_{obs}} \quad (5)$$

where ∇^2 is the Laplacian operator defined on fault slip surface coordinates, and ϵ is the damping parameter. As shown in Fig. S15c-h, the larger the damping ϵ, the smoother the solution. Fig. S15a shows that shallow slip deficit values vary widely as a function of ϵ, from 13% to 57%. Unsurprisingly, models with little regularization (e.g., $\epsilon \sim 0.1$) are quite consistent with our Bayesian solution, including in terms of shal-
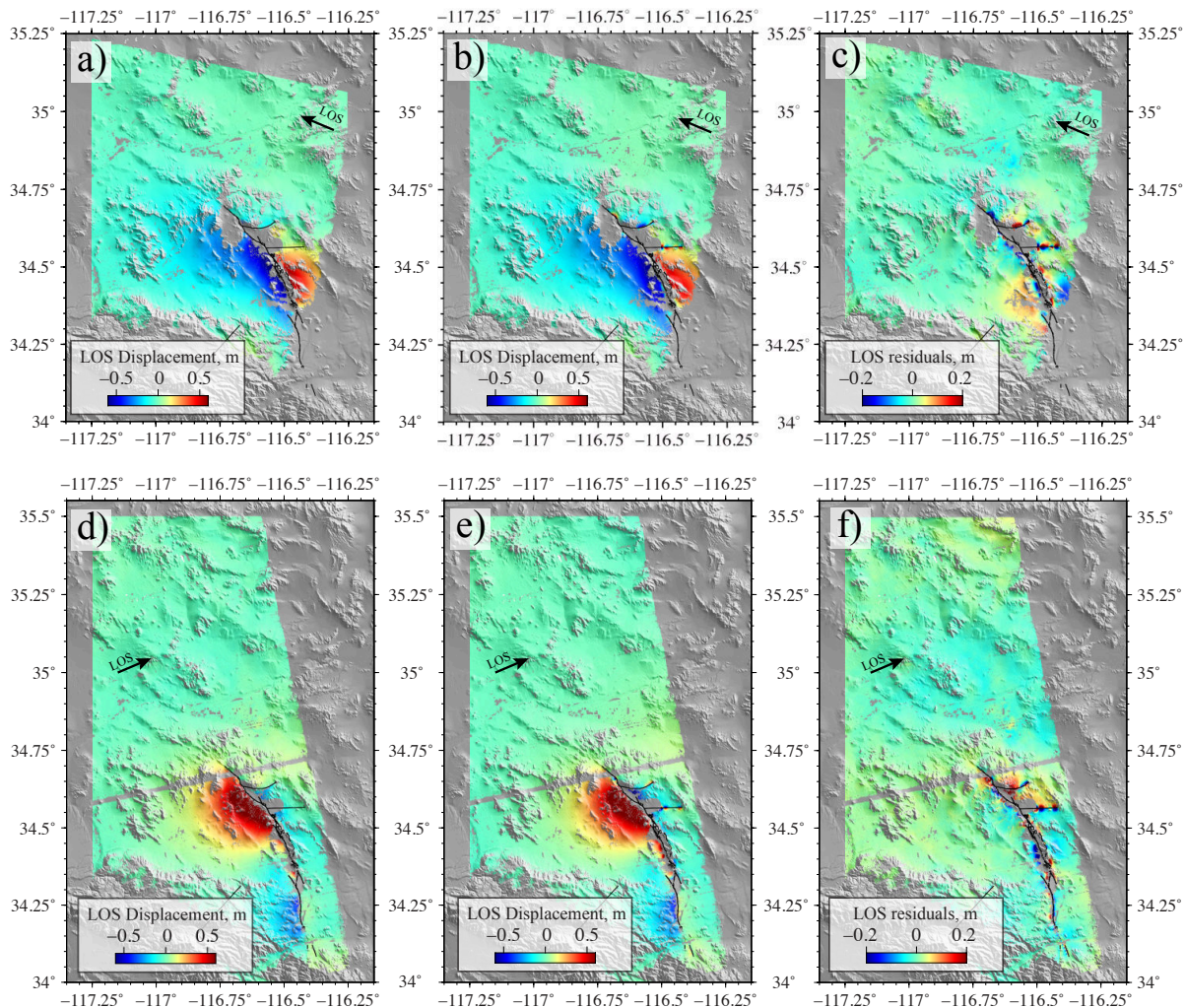
Figure 6. Model performance for InSAR. **(a, d)** InSAR observations. **(b, e)** Predictions for the posterior mean model. **(c, f)** InSAR residuals of the descending (top) and ascending (bottom) tracks.

low slip deficit. The choice of ϵ is to a large extent arbitrary. However, we still notice large variations of the SSD by selecting a few models localized around the corner of the L-curve (Fig. S15b). Such a strong dependence on ϵ complicates any interpretation of the results of smoothed models in terms of shallow slip deficit. Of course, other factors can possibly impact the inferred slip distribution such as the choice of fault geometry or the datasets included in the inversion. As shown in Table S2, we do not see any clear direct relationship between used datasets and the inferred SSD. For example, both Fialko (2004b) and Xu et al. (2016) used observations similar to ours but with different estimates of the SSD. Such variability do not seem to be explained by the assumed fault parametrization since both studies used a complex geometry similar to the one we use (cf., Table S2). Another example is Cohee & Beroza (1994) and Zeng & Anderson (2000) that are based on similar fault planes and datasets but with different SSD estimates. Inversion results can be affected by other parameters such as fault discretization, data weighting, and elastic structure (whose uncertainty is accounted for in the present study). A better understanding of the variability of previous models would require extensive tests using different geometries, datasets, and weighting schemes, which is beyond the scope of this study.

Different artifacts affecting co-seismic slip models are often proposed to explain the shallow slip deficit inferred for large strike-slip earthquakes. One of them is the inelastic strain in the vicinity of the fault that is usually unaccounted in finite-fault inversions (e.g., Simons et al. 2002, Fialko et al. 2005). Such inelastic response can indeed bias slip inversions that are based on elastic Green's functions and artificially decrease the amount of slip at shallow depth (Kaneko & Fialko 2011). However, as reported by Milliner et al. (2015), inelastic strain for the 1992 Landers earthquake is limited to a relatively narrow region around the fault (e.g., within ~65 m of the fault trace in Fig. 8c). To avoid any strong bias due to our elas-
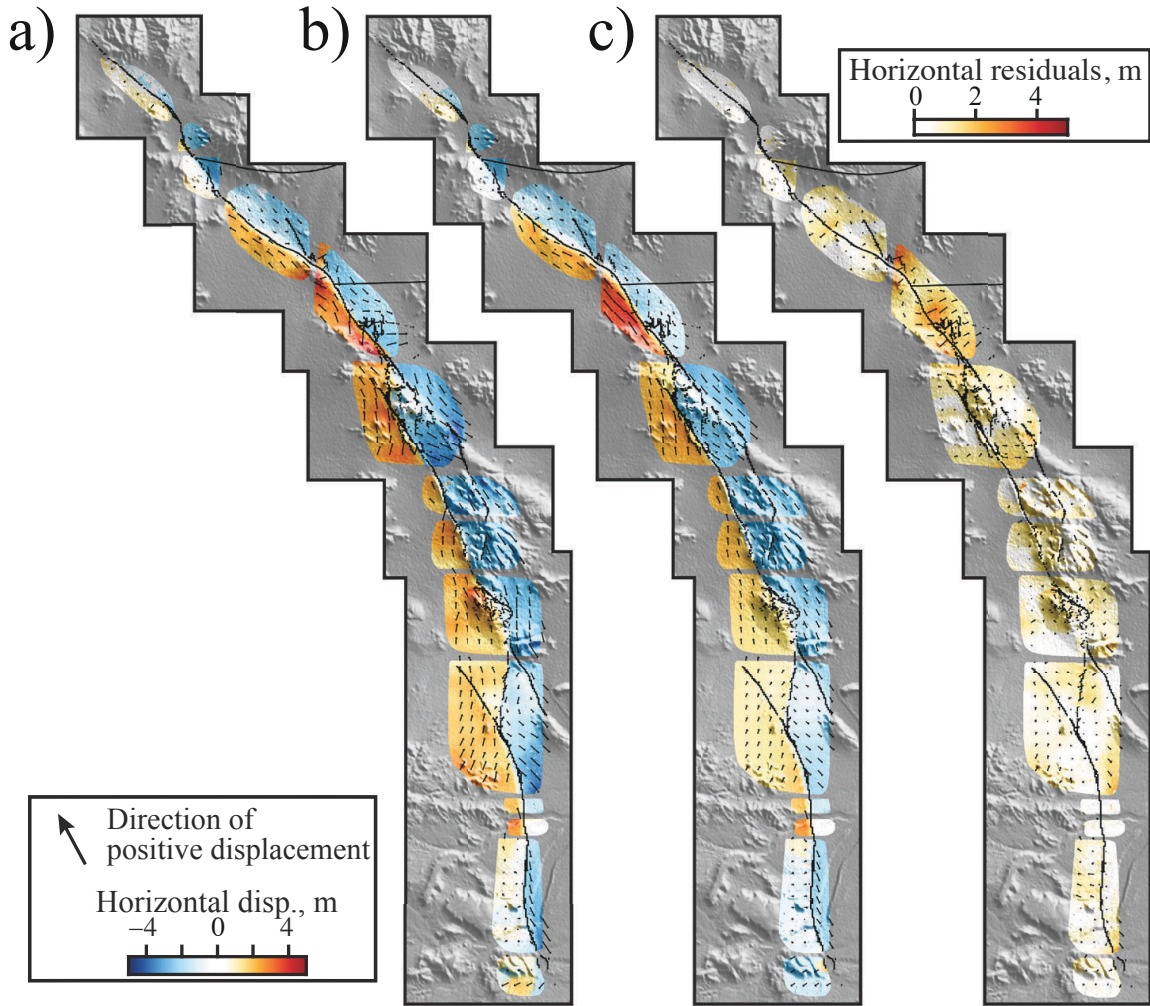
Figure 7. Model performance for optical image correlation data. **(a)** Observations. **(b)** Predictions for the posterior mean model. **(c)** Residuals. Positive displacements are toward the north-west (see arrow in the legend).

tic assumption and reduce modeling errors due to fault discretization at shallow depth, we have removed displacement data within a minimum distance of 300 m from the fault trace (see section 2.3). This procedure is roughly equivalent to localizing the inelastic contribution of the strain field onto an idealized fault plane (Dahlen & Tromp 1998). Although removing near-fault pixels should reduce artifacts due to inelastic effects, unaccounted lateral heterogeneities due to accumulated damage around the fault can also have a significant impact on surface deformation patterns and by extension on the inverted slip distribution (Barbot et al. 2008).

The fault zone is often regarded as a highly deformed core surrounded by a more or less broad damage zone of reduced stiffness (e.g. Chester et al. 1993, Ben-Zion & Sammis 2003, Mitchell & Faulkner 2009, Dor et al. 2006). The damage zone consists of cracks and microfractures in the host rock and can be associated with secondary faults reducing the elastic strain released on the main rupture interface (Chester & Chester 1998, Dieterich & Smith 2009). Such secondary

cracks have been reported around the Landers fault system (McGill & Rubin 1999). An example is given in Fig. 8, showing two secondary ruptures (labeled F1 and F2) visible in optical correlation images near the Emerson Valley fault. Such off-fault ruptures are not accounted for in our slip model presented in Fig. 4.

To investigate the properties of the damage zone and secondary ruptures, we analyze a profile across the fault using simple vertical elastic screw dislocations embedded in a compliant fault zone (Segall 2010). Using a Metropolis algorithm, we invert for the slip distribution on each fault, a compliant zone half-width and an effective shear modulus contrast μ_1/μ_0 (where μ_1 is the shear modulus of the fault zone while μ_0 is the modulus of the surrounding crust). The compliant zone half-width and shear modulus ratio being typical Jeffreys parameters (Tarantola 2005), they are sampled in the logarithmic domain. To avoid any effect of off-fault inelasticity, we remove the data within 65 m of the fault, which is consistent with fault-width measurements by Milliner et al. (2015) at this
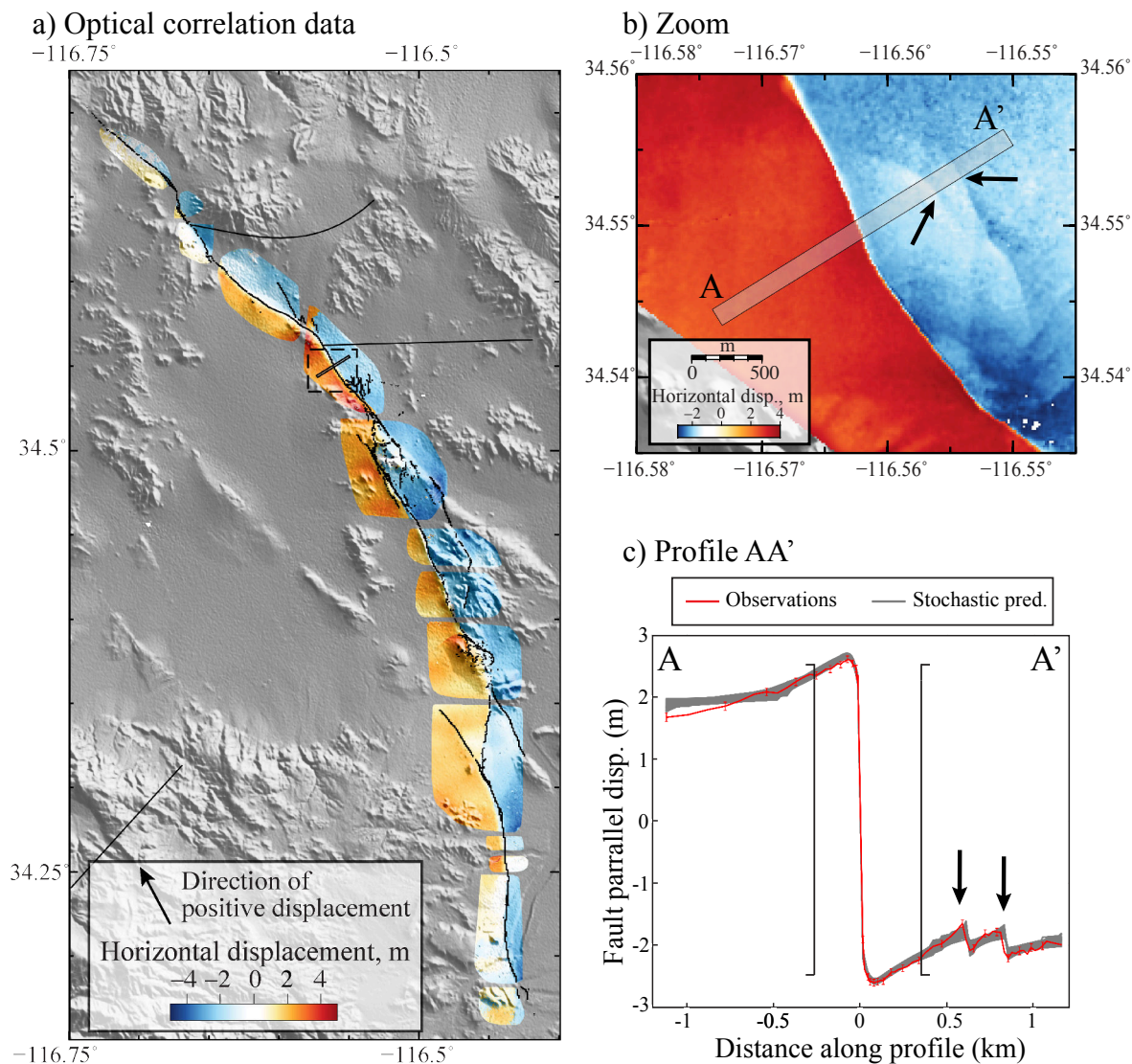
Figure 8. Modeling of Near-field deformation data. **(a)** Overall view of optical correlation data. The profile shown in (c) is localized with a black line. **(b)** Close up view of near-field data. Grey rectangle indicate the location of the profile shown in (c). **(c)** Comparison between observed displacement (in red) and the stochastic predictions (in grey). Black arrows labeled F1 and F2 in (b) and (c) highlight two small secondary ruptures visible in the data. These small ruptures are incorporated in our modeling approach assuming two vertical dislocations. Data inside the black brackets are not used in the inversion of the full 3D slip distribution presented in Fig. 4 to reduce the impact of inelastic effects in the vicinity of the main rupture.

Table 1. Shallow slip deficit estimated for different fault segments and for the whole rupture. A zero or negative SSD means that there is no deficit. A SSD value of 50% means that there is twice more slip at depth than at the surface.

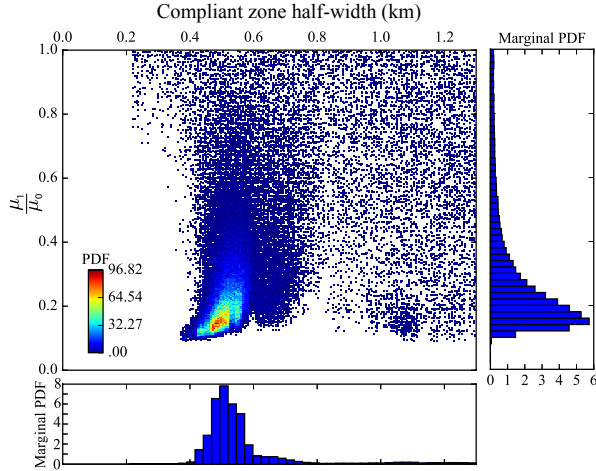| Fault segment	Mean SSD	95% conf. interval	Probability than SSD is greater or equal than...		
			0%	25%	50%
Emerson and Camp Rock	2.6%	-25.1% - 33.5%	62%	3.1%	0%
Johnson Valley	25.4%	-3.8% - 57.6%	94%	58.2%	<1%
Homestead Valley	51.7%	42.7% - 61.9%	100%	97.0%	67.5%
All faults combined	40.9%	35.2% - 47.3%	100%	99.9%	<1%
All faults combined taking into account a compliant zone	29.6%	14.32% - 46.4%	99.6%	75.8%	<1%

Figure 9. Posterior joint probability distribution of the compliant zone half-width and shear modulus ratio. Dots are model samples that are coloured according to the PDF value. Blue histograms are marginal PDFs for both parameters.

location. The results presented in Fig. 8(c) indicate very shallow secondary ruptures with 32 ± 8 cm and 36 ± 5 cm of slip down to 84 ± 30 m and 180 ± 40 m respectively for faults F1 and F2. Although such slip amplitudes are not negligible, these off-fault dislocations are relatively shallow and thus represent only 3.3% of the total seismic slip inferred from the surface down to 0.5 km. Of course, these measurements are only valid locally since the properties of secondary faults might vary significantly along the main rupture (Lewis & Ben-Zion 2010, Milliner et al. 2015, Thomas et al. 2017).

The results shown in Fig. 9 highlight the existence of a $\sim$1.1 km wide compliant zone around this part of the fault. Although there is some correlation between the compliant zone width and rigidity, our solution indicates that shear modulus can be reduced by as much as a factor $\sim$5 within the damage zone (i.e., a shear modulus ratio of $\sim$0.2). This estimate is consistent with measurements from guided seismic waves (Li et al. 2007, 1994, Peng et al. 2003) that indicate shear modulus ratios between 0.1 and 0.4, corresponding to 80% of our models. On the other hand, these studies suggest relatively small damage zone widths of a few hundred meters, which is narrower than our estimates.

Using the aftershock catalog of Hauksson et al. (2012), we compare our estimates with the distribution of seismicity around the main fault, which is another indicator of distributed damage in the host rock (Amitrano 2006, Powers & Jordan 2010). As shown in Fig. 10(a), we select two profiles across the main rupture surrounding the southern antithetic fault to avoid any bias due to events located on this segment. Following Powers & Jordan (2010), we compute the horizontal density $\nu(x)$ of seismicity where x is the fault normal distance, and assume a power law decay of the form

$$\nu(x) = \nu_0 \left(1 + \frac{x^2}{d^2} \right)^{-\gamma/2} \qquad (6)$$

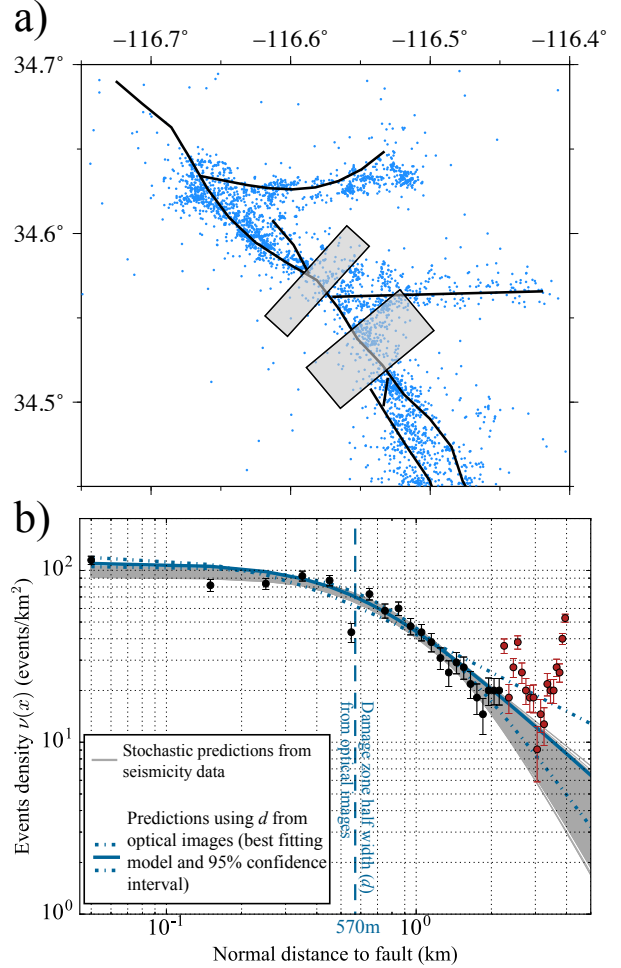where ν_0 is the aftershock density at $x = 0$, d is the damage

Figure 10. Distribution of seismicity across the fault. **(a)** Our parametrized fault trace is indicated with thick black lines. Blue dots are aftershock epicenters from Hauksson et al. (2012). Grey rectangles illustrate the location of profiles used for the seismicity density analysis. **(b)** Seismicity density as a function of fault normal distance. Densities are computed over the two stacked profiles using 100 m wide distance bins. Black circles are resulting event density measurements used in the power-law inversion. Red circles are observations not included in the inversion since they correspond to events located at distance larger than $\sim$2 km that may be partly linked to the southern antithetic fault segment. The 1-σ error bars were obtained by computing the standard deviation of density in each bin from 1000 random catalogs generated according to event location uncertainties.

zone half-width and γ is the asymptotic roll-off of the seismicity away from the fault. Using a Metropolis inversion scheme, we then sample ν_0, d, and γ given the seismicity density, $\nu(x)$. Comparison between observations and stochastic predictions are shown in Fig. 10(b) and the full posterior PDFs for the 3 parameters are shown in Fig. S16. Although the posterior mean damage-zone half-width $d \sim 800$ m is larger than what is inferred from optical images ($d \sim 570$ m), an inversion with a fixed $d = 570$ m also explains the data reasonably well (cf. Fig. 10(b)).
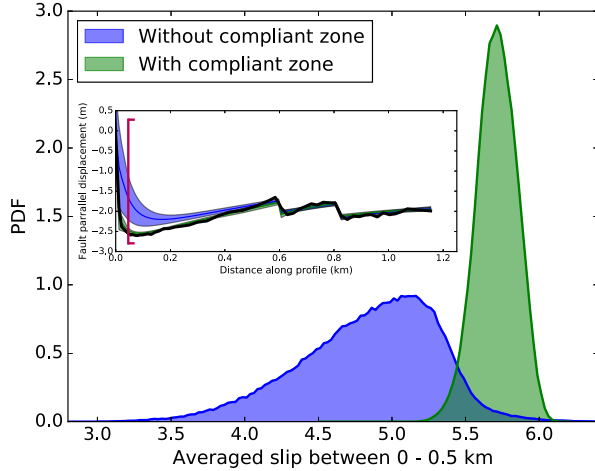
Figure 11. Comparison between shallow slip posterior PDFs assuming an homogeneous half-space (in blue) and accounting for a damage zone of reduced stiffness (in green). The inset shows stochastic predictions for both inversions. Observations are plotted as a thin black line. Blue results are inferred without the data inside the brackets in Fig. 8(c) and green results without the data inside the red brackets at ±65 m

To estimate the impact of the damage zone on the inverted slip distribution, we also invert the fault-parallel displacement profile of Fig. 8(c) without a compliant zone and after removing the data within 300 m of the fault (i.e. the same way it is done in our main slip inversion). The posterior PDFs of shallow slip and stochastic predictions with and without accounting for the damage zone are shown in Fig. 11. Although far field deformation is well-predicted in both inversions, predictions neglecting a compliant zone fail to reproduce near-fault observations and underestimate slip at shallow depth. On aver-
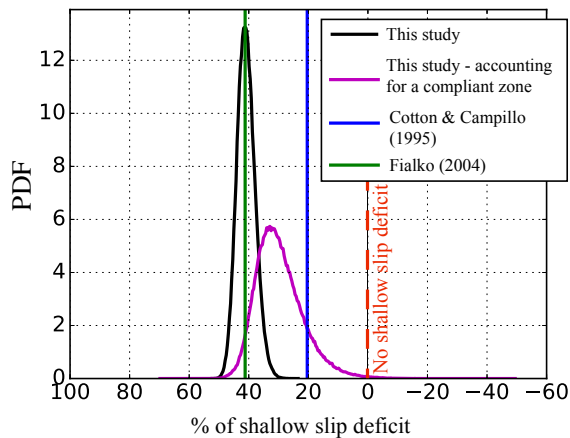

Figure 12. Overall shallow slip deficit (SSD). The black PDF indicate the SSD for the overall rupture presented in Fig. 4. The purple PDF is the SSD corrected from the effect of the damage zone with reduced stiffness. Blue and Green vertical lines are the SSD for two published models (Cotton & Campillo 1995, Fialko 2004*b*).

age, accounting for the compliant zone increases shallow slip by a factor of 1.2. On the other hand, neglecting lateral shear modulus heterogeneities will systematically lead to smaller slip (with a probability of 98%). To roughly estimate the effect of the damage zone, we can empirically correct the surface mean slip of the Landers rupture by factors drawn from posterior PDFs with and without accounting for the compliant zone. Results presented in Fig. 12 and Table 1, indicate that this significantly reduces the overall shallow slip deficit from 41% to 27%. These results should, however, be considered with caution, as the damage behavior can vary significantly along the fault (Lewis & Ben-Zion 2010). We tried to conduct similar experiments in other locations on the fault but did not obtain reliable constraints on the compliant zone parameters (see for example Figs S17 and S18). Even if damage properties can widely vary along the fault, such structures will necessarily impact slip estimated at shallow depth, thereby reducing the inferred shallow deficit.

5   CONCLUSION

We used an extensive geodetic dataset, careful uncertainty estimates and a realistic fault geometry to produce a stochastic finite-fault model of the Landers earthquake. Our Bayesian approach to the inversion has two main advantages: (1) the solution is not biased by any kind of smoothing and (2) posterior parameter uncertainties are available and provide valuable information on the validity of the model. The predictions from our solution agree well with various observations.

Consistent with previous studies, our solution indicates a substantial shallow slip deficit that is particularly pronounced for the Homestead Valley Fault. We argue that part of this deficit results from unmodeled lateral heterogeneities in shear modulus, corresponding to a damage zone surrounding the fault. Using high resolution optical correlation images, we highlight a ∼1 km wide damage zone on the Emerson Valley Fault responsible for an apparent reduction in shallow slip by a factor ∼1.2. Our results also show the presence of secondary ruptures with significant slip amplitudes at shallow depth. By reducing the elastic strain on the main fault, these features also contribute to the apparent slip deficit budget.

Although we do not include data in the immediate vicinity of the fault where inelastic behavior is commonly observed, we cannot rule out that some wide plastic deformation is included in our inversion and participates in the observed deficit. Following the same procedure, other near-field displacement data of large strike-slip earthquakes could provide new insights on fault zone properties and their link to co-seismic slip distribution.

6   ACKNOWLEDGMENT

References

Amitrano, D. (2006), 'Rupture by damage accumulation in rocks', *International Journal of Fracture* **139**(3), 369–381.

Ayoub, F., Leprince, S. & Avouac, J.-P. (2009), 'Co-registration and correlation of aerial photographs for ground deformation measurements', *ISPRS Journal of Photogrammetry and Remote Sensing* **64**(6), 551–560.

Barbot, S., Fialko, Y. & Sandwell, D. (2008), 'Effect of a compliant fault zone on the inferred earthquake slip distribution', *Journal of Geophysical Research: Solid Earth* **113**(B6).

Ben-Zion, Y. & Sammis, C. G. (2003), Characterization of fault zones, *in* 'Seismic Motion, Lithospheric Structures, Earthquake and Volcanic Sources: The Keiiti Aki Volume', Springer, pp. 677–715.

Candela, T., Renard, F., Schmittbuhl, J., Bouchon, M. & Brodsky, E. E. (2011), 'Fault slip distribution and fault roughness', *Geophysical Journal International* **187**(2), 959968.

Chester, F. M. & Chester, J. S. (1998), 'Ultracataclasite structure and friction processes of the Punchbowl fault, San Andreas system, California', *Tectonophysics* **295**(1), 199–221.

Chester, F. M., Evans, J. P. & Biegel, R. L. (1993), 'Internal structure and weakening mechanisms of the San Andreas fault', *Journal of Geophysical Research: Solid Earth* **98**(B1), 771–786.

Cohee, B. P. & Beroza, G. C. (1994), 'Slip distribution of the 1992 Landers earthquake and its implications for earthquake source mechanics', *Bulletin of the Seismological Society of America* **84**(3), 692–712.

Cotton, F. & Campillo, M. (1995), 'Frequency domain inversion of strong motions: application to the 1992 Landers earthquake', *Journal of Geophysical Research: Solid Earth* **100**(B3), 3961–3975.

Dahlen, F. & Tromp, J. (1998), *Theoretical global seismology*, Princeton university press.

Dieterich, J. H. & Smith, D. E. (2009), 'Nonplanar faults: Mechanics of slip and off-fault damage', *Pure and Applied Geophysics* **166**(10-11), 1799–1815.

Dor, O., Ben-Zion, Y., Rockwell, T. K. & Brune, J. (2006), 'Pulverized rocks in the Mojave section of the San Andreas Fault Zone', *Earth and Planetary Science Letters* **245**(3), 642–654.

Duputel, Z., Agram, P. S., Simons, M., Minson, S. E. & Beck, J. L. (2014), 'Accounting for prediction uncertainty when inferring subsurface fault slip', *Geophysical Journal International* **197**(1), 464–482.

Fialko, Y. (2004*a*), 'Evidence of fluid-filled upper crust from observations of postseismic deformation due to the 1992 Mw7.3 Landers earthquake', *Journal of Geophysical Research: Solid Earth* **109**(B8).

Fialko, Y. (2004*b*), 'Probing the mechanical properties of seismically active crust with space geodesy: Study of the coseismic deformation due to the 1992 Mw7.3 Landers (southern California) earthquake', *Journal of Geophysical Research: Solid Earth* **109**(B3).

Fialko, Y., Sandwell, D., Agnew, D., Simons, M., Shearer, P. & Minster, B. (2002), 'Deformation on nearby faults

induced by the 1999 Hector Mine earthquake', *Science* **297**(5588), 1858–1862.

Fialko, Y., Sandwell, D., Simons, M. & Rosen, P. (2005), 'Three-dimensional deformation caused by the Bam, Iran, earthquake and the origin of shallow slip deficit', *Nature* **435**(7040), 295.

Freymueller, J., King, N. & Segall, P. (1994), 'The co-seismic slip distribution of the Landers earthquake', *Bulletin of the Seismological Society of America* **84**(3), 646–659.

Hansen, P. C. (1998), *Rank-deficient and discrete ill-posed problems: numerical aspects of linear inversion*, SIAM.

Hartzell, S. H. & Heaton, T. H. (1983), 'Inversion of strong ground motion and teleseismic waveform data for the fault rupture history of the 1979 Imperial Valley, California, earthquake', *Bulletin of the Seismological Society of America* **73**(6A), 1553–1583.

Hauksson, E., Yang, W. & Shearer, P. M. (2012), 'Waveform relocated earthquake catalog for southern California (1981 to June 2011)', *Bulletin of the Seismological Society of America* **102**(5), 2239–2244.

Hernandez, B., Cotton, F. & Campillo, M. (1999), 'Contribution of radar interferometry to a two-step inversion of the kinematic process of the 1992 Landers earthquake', *Journal of Geophysical Research* **104**(B6), 13083.

Hudnut, K. W., Bock, Y., Cline, M., Fang, P., Feng, Y., Freymueller, J., Ge, X., Gross, W., Jackson, D., Kim, M. et al. (1994), 'Co-seismic displacements of the 1992 Landers earthquake sequence', *Bulletin of the Seismological society of America* **84**(3), 625–645.

Jolivet, R., Duputel, Z., Riel, B., Simons, M., Rivera, L., Minson, S. E., Zhang, H., Aivazis, M. a. G., Ayoub, F. & Leprince, S. (2014), 'The 2013 Mw 7.7 Balochistan earthquake: Seismic potential of an accretionary wedge', *Bulletin of the Seismological Society of America* **104**(2), 1020–1030.

Kaneko, Y. & Fialko, Y. (2011), 'Shallow slip deficit due to large strike-slip earthquakes in dynamic rupture simulations with elasto-plastic off-fault response', *Geophysical Journal International* **186**(3), 1389–1403.

Kohler, M., Magistrale, H. & Clayton, R. (2003), 'Mantle heterogeneities and the SCEC reference three-dimensional seismic velocity model version 3', *Bulletin of the Seismological Society of America* **93**(2), 757–774.

Lewis, M. A. & Ben-Zion, Y. (2010), 'Diversity of fault zone damage and trapping structures in the Parkfield section of the San Andreas Fault from comprehensive analysis of near fault seismograms', *Geophysical Journal International* **183**(3), 1579–1595.

Li, H., Zhu, L. & Yang, H. (2007), 'High-resolution structures of the Landers fault zone inferred from aftershock waveform data', *Geophysical Journal International* **171**(3), 1295–1307.

Li, Y.-G., Vidale, J. E., Aki, K., Marone, C. J., Lee, W. H. et al. (1994), 'Fine structure of the Landers fault zone: segmentation and the rupture process', *Science* pp. 367–367.

Lohman, R. B. & Simons, M. (2005), 'Some thoughts on the use of InSAR data to constrain models of surface deformation: Noise structure and data downsampling', *Geochemistry, Geophysics, Geosystems* **6**(1).

Mai, P. M., Schorlemmer, D., Page, M., Ampuero, J.-P.,

Asano, K., Causse, M., Custodio, S., Fan, W., Festa, G., Galis, M. et al. (2016), 'The earthquake-source inversion validation (SIV) project', *Seismological Research Letters* .

McGill, S. F. & Rubin, C. M. (1999), 'Surficial slip distribution on the central Emerson fault during the June 28, 1992, Landers earthquake, California', *Journal of Geophysical Research: Solid Earth* **104**(B3), 4811–4833.

Milliner, C., Sammis, C., Allam, A., Dolan, J., Hollingsworth, J., Leprince, S. & Ayoub, F. (2016), 'Resolving fine-scale heterogeneity of co-seismic slip and the relation to fault structure', *Scientific reports* **6**, srep27201.

Milliner, C. W., Dolan, J. F., Hollingsworth, J., Leprince, S., Ayoub, F. & Sammis, C. G. (2015), 'Quantifying near-field and off-fault deformation patterns of the 1992 Mw 7.3 Landers earthquake', *Geochemistry, Geophysics, Geosystems* **16**(5), 1577–1598.

Minson, S., Simons, M. & Beck, J. (2013), 'Bayesian inversion for finite fault earthquake source models I-Theory and algorithm', *Geophysical Journal International* **194**(3), 1701–1726.

Mitchell, T. & Faulkner, D. (2009), 'The nature and origin of off-fault damage surrounding strike-slip fault zones with a wide range of displacements: a field study from the Atacama fault system, northern Chile', *Journal of Structural Geology* **31**(8), 802–816.

Murray, M., Savage, J., Lisowski, M. & Gross, W. (1993), 'Coseismic displacements: 1992 Landers, California, earthquake', *Geophysical research letters* **20**(7), 623–626.

Olson, A. H. & Apsel, R. J. (1982), 'Finite faults and inverse theory with applications to the 1979 Imperial Valley earthquake', *Bulletin of the Seismological Society of America* **72**(6A), 1969–2001.

Ortega, F. (2013), Aseismic Deformation in Subduction Megathrusts: Central Andes and North-East Japan, PhD thesis, California Institute of Technology.

Peltzer, G., Rosen, P., Rogez, F. & Hudnut, K. (1998), 'Poroelastic rebound along the Landers 1992 earthquake surface rupture', *Journal of Geophysical Research: Solid Earth* **103**(B12), 30131–30145.

Peng, Z., Ben-Zion, Y., Michael, A. J. & Zhu, L. (2003), 'Quantitative analysis of seismic fault zone waves in the rupture zone of the 1992 Landers, California, earthquake: evidence for a shallow trapping structure', *Geophysical Journal International* **155**(3), 1021–1041.

Powers, P. M. & Jordan, T. H. (2010), 'Distribution of seismicity across strike-slip faults in California', *Journal of Geophysical Research: Solid Earth* **115**(B5).

Rosen, P. A., Hensley, S., Peltzer, G. & Simons, M. (2004), 'Updated repeat orbit interferometry package released', *Eos, Transactions American Geophysical Union* **85**(5), 47–47.

Roux, P., Wathelet, M. & Roueff, A. (2011), 'The San Andreas Fault revisited through seismic-noise and surface-wave tomography', *Geophysical Research Letters* **38**(13).

Savage, J. & Burford, R. (1970), 'Accumulation of tectonic strain in California', *Bulletin of the Seismological Society of America* **60**(6), 1877–1896.

Savage, J. C. & Svarc, J. L. (1997), 'Postseismic deformation

associated with the 1992 M=7.3 Landers earthquake, southern California', *Journal of Geophysical Research: Solid Earth* **102**(B4), 75657577.

Segall, P. (2010), *Earthquake and volcano deformation*, Princeton University Press.

Segall, P. & Harris, R. (1987), 'Earthquake deformation cycle on the San Andreas Fault near Parkfield, California', *Journal of Geophysical Research: Solid Earth* **92**(B10), 1051110525.

Segall, P. & Pollard, D. (1980), 'Mechanics of discontinuous faults', *Journal of Geophysical Research: Solid Earth* **85**(B8), 4337–4350.

Shen, Z.-K., Jackson, D. D., Feng, Y., Cline, M., Kim, M., Fang, P. & Bock, Y. (1994), 'Postseismic deformation following the Landers earthquake, California, 28 June 1992', *Bulletin of the Seismological Society of America* **84**(3), 780791.

Sieh, K., Jones, L., Hauksson, E., Hudnut, K., Eberhart-Phillips, D., Heaton, T., Hough, S., Hutton, K., Kanamori, H., Lilje, A. et al. (1993), 'Near-field investigations of the Landers earthquake sequence, April to July 1992', *Science* **260**, 171–171.

Simons, M., Fialko, Y. & Rivera, L. (2002), 'Coseismic deformation from the 1999 Mw 7.1 Hector Mine, California, earthquake as inferred from InSAR and GPS observations', *Bulletin of the Seismological Society of America* **92**(4), 1390–1402.

Tarantola, A. (2005), *Inverse problem theory and methods for model parameter estimation*, SIAM.

Thomas, M. Y., Bhat, H. S. & Klinger, Y. (2017), 'Effect of Brittle Off-Fault Damage on Earthquake Rupture Dynamics', *Fault Zone Dynamic Processes: Evolution of Fault Properties During Seismic Rupture* **227**, 255.

Tse, S. T. & Rice, J. R. (1986), 'Crustal earthquake instability in relation to the depth variation of frictional slip properties', *Journal of Geophysical Research: Solid Earth* **91**(B9), 9452–9472.

Vallage, A., Klinger, Y., Grandin, R., Bhat, H. & Pierrot-Deseilligny, M. (2015), 'Inelastic surface deformation during the 2013 Mw 7.7 Balochistan, Pakistan, earthquake', *Geology* **43**(12), 1079–1082.

Wald, D. J. & Heaton, T. H. (1994), 'Spatial and temporal distribution of slip for the 1992 Landers, California, earthquake', *Bulletin of the Seismological Society of America* **84**(3), 668–691.

Xu, X., Tong, X., Sandwell, D. T., Milliner, C. W., Dolan, J. F., Hollingsworth, J., Leprince, S. & Ayoub, F. (2016), 'Refining the shallow slip deficit', *Geophysical Journal International* **204**(3), 1867–1886.

Zeng, Y. & Anderson, J. (2000), *Evaluation of numerical procedures for simulating near-fault long-period ground motions using Zeng method, Report 2000/01 to the PEER Utilities Program , available at http://peer.berkeley.edu*.

Zhu, L. & Rivera, L. A. (2002), 'A note on the dynamic and static displacements from a point source in multilayered media', *Geophysical Journal International* **148**(3), 619–627.

Zigone, D., Ben-Zion, Y., Campillo, M. & Roux, P. (2015), 'Seismic tomography of the Southern California plate boundary region from noise-based Rayleigh and Love waves', *Pure and Applied Geophysics* **172**(5), 1007–1032.